(This is a sample cover image for this issue. The actual cover is not yet available at this time.)

Synthetic Metals 162 (2012) 1558–1565

Contents lists available at SciVerse ScienceDirect

Synthetic Metals

journal homepage: www.elsevier.com/locate/synmet

Three 3D organic–inorganic hybrid heterometallic polyoxotungstates assembled from 1:2-type $[Ln(\alpha\text{-}SiW_{11}O_{39})_2]^{13-}$ silicotungstates and $[Cu(dap)_2]^{2+}$ linkers

Jie Luo[a,b], Chunli Leng[b], Lijuan Chen[a,b,*], Jing Yuan[a], Huiying Li[a], Junwei Zhao[a,c,*]

[a] Institute of Molecular and Crystal Engineering, College of Chemistry and Chemical Engineering, Henan University, Kaifeng, Henan 475004, PR China
[b] Basic Experiment Teaching Center, Henan University, Kaifeng, Henan 475004, PR China
[c] State Key Laboratory of Structural Chemistry, Fujian Institute of Research on the Structure of Matter, Chinese Academy of Sciences, Fuzhou, Fujian 350002, PR China

ARTICLE INFO

Article history:
Received 5 May 2012
Received in revised form 13 June 2012
Accepted 22 June 2012

Keywords:
Polyoxometalate
Silicotungstate
Luminescence
Magnetism

ABSTRACT

Three organic–inorganic hybrid monolacunary Keggin silicotungstate-based 3d–4f heterometallic derivatives $NaH[Cu(dap)_2(H_2O)][Cu(dap)_2]_{4.5}[Ln(\alpha\text{-}SiW_{11}O_{39})_2]\cdot 7H_2O$ (Ln = Sm^{III} for **1**, Dy^{III} for **2**, Gd^{III} for **3**) have been prepared by the hydrothermal reaction of $Na_{10}[A\text{-}\alpha\text{-}SiW_9O_{34}]\cdot 18H_2O$, $CuCl_2\cdot 2H_2O$, $LnCl_3$ and dap (dap = 1,2-diaminopropane) and characterized by elemental analyses, IR spectra and X-ray single-crystal diffraction. **1**–**3** display the novel 3D Cu^{II}–Ln^{III} heterometallic frameworks with the scarce 5-connected ($4^6.6^4$) topology and their common features are that they all consist of 1:2-type $[Ln(\alpha\text{-}SiW_{11}O_{39})_2]^{13-}$ subunits and $[Cu(dap)_2]^{2+}$ connectors. To the best of our knowledge, **1**–**3** represent the rare 3D organic–inorganic hybrid Keggin silicotungstate-based 3d–4f heterometallic derivatives. In addition, the photoluminescence properties of **1** and **2** have been investigated and the magnetic susceptibilities of **1**–**3** have been measured.

1. Introduction

Polyoxometalates (POMs), as a unique class of anionic metal-oxygen clusters, have attracted considerable attention in recent years owing to not only their remarkable variety of structures but also their potential applications in catalysis, photochemistry, electrochemistry and magnetism [1–5]. Among them, Keggin-type POMs can often act as useful inorganic polydentate ligands, which can be functionalized by transition-metal (TM) or lanthanide (Ln) cations, forming TM-substituted POMs (TMSPs) or Ln-substituted POMs (LSPs) [6–11]. Currently, exploring and discovering novel 3d–4f heterometallic Keggin-type POMs remain a severe challenge and a longstanding task although some similar species have been successively synthesized [12–21] such as $[\{Ln(PW_{11}O_{39})_2\}\{Cu_2(bpy)_2(\mu\text{-}ox)\}]^{9-}$ (Ln = La^{III}, Pr^{III}, Eu^{III}, Gd^{III}, Yb^{III}) [12], $[K\subset\{FeCe(AsW_{10}O_{38})(H_2O)_2\}_3]^{14-}$ [13], $[\{Ce(\alpha\text{-}PW_{11}O_{39})_2\}Cu(en)_2]^{9-}$ [14], $[Cu(en)_2\{Er(\alpha\text{-}PW_{11}O_{39})_2\}Cu(en)_2]^{7-}$ [14], $\{[Cu(en)_2]_2[Na_2(H_2O)_{1.75}][K(H_2O)_3][Dy_2(H_2O)_2(GeW_{11}O_{39})_3]\}^{11-}$ [15], $\{[Cu(en)_2]_2[Ce(\alpha\text{-}PW_{11}O_{39})_2]\}^{6-}$ [16], $\{[Cu(dap)_2]_{4.5}[Dy(\alpha\text{-}PW_{11}O_{39})_2]\}^{2-}$ [16], $\{[Cu(en)_2]_{1.5}[Cu(en)(2,2'\text{-bipy})(H_2O)n]Ln[(\alpha\text{-}PW_{11}O_{39})_2]\}^{6-}$ (Ln = Ce^{III}, Pr^{III}) [17], $\{[Cu(en)_2]_2(H_2O)[Cu(en)(2,2'\text{-bipy})]Ln[(\alpha\text{-}HPW_{11}O_{39})_2]\}^{4-}$ (Ln = Gd^{III}, Tb^{III}, Er^{III}) [17] and $\{[Cu(en)_2]_{1.5}[Cu(en)(2,2'\text{-bipy})]Nd[(\alpha\text{-}H_5PW_{11}O_{39})_2]\}^{3-}$ [17]. However, reports on 3d–4f heterometallic Keggin-type silicotungstates (STs) remain very limited. During the course of 2007–2011, Wang and coworkers addressed several inorganic 3d–4f heterometallic STs $[\{Ce(H_2O)_7\}_2Mn_4Si_2W_{18}O_{68}(H_2O)_2]^{6-}$ [22], $\{Nd_2(H_2O)_{12}Cu_4(H_2O)_2(SiW_9O_{34})_2\}^{6-}$ [23] and $[K_9Ln_6Fe_6(H_2O)_{12}(SiW_{10}O_{38})_6]^{26-}$ (Ln = Dy^{III}, Tb^{III}) [24]. In 2009–2010, three novel $\{LnCu_3(OH)_3O\}$-cubane inserted STs $\{[Cu(en)_2(H_2O)][(Cu(en)(OH))_3Ln(SiW_{11}O_{39})(H_2O)]\}_2\cdot 20H_2O$ (Ln = La^{III}, Gd^{III}, Eu^{III}) and a 1D double-chain $[(\gamma\text{-}SiW_{10}O_{36})_2(Cr(OH)(H_2O))_3(La(H_2O)_7)_2]^{4-}$ were isolated by Mialane et al. [25,26]. Recently, Niu's group obtained a family of novel 3d–4f heterometallic ST hybrids $\{[Cu(en)_2]_{1.5}Ln[(\alpha\text{-}SiW_{11}O_{39})_2]\}_2^{20-}$ (Ln = Gd^{III}, Tb^{III}, Dy^{III}, Er^{III}, Lu^{III}) [27], $\{[Cu(en)_2]_{1.5}Ln[(\alpha\text{-}SiW_{11}O_{39})]\}^{2-}$ (Ln = La^{III}, Ce^{III}) [27], $Cu(en)_2(H_2O)]_2\{[Cu(en)_2]_2[Cu(pzda)_2][(\alpha\text{-}H_2SiW_{11}O_{39})Ce(H_2O)]_2\}\cdot nH_2O$ [28] and $[Cu(en)_2(H_2O)]_2\{[Cu(en)_2][Cu(en)_2(H_2O)][(\alpha\text{-}SiW_{11}O_{39})Ln(H_2O)(pzda)]\}_2^{2-}$ (Ln = Y^{III}, Dy^{III}, Yb^{III}, Lu^{III}) [28]. Very recently, we have expanded our research to prepare novel high-dimensional organic–inorganic hybrid 3d–4f heterometallic STs by reaction of $Na_{10}[A\text{-}\alpha\text{-}SiW_9O_{34}]\cdot 18H_2O$, $CuCl_2\cdot 2H_2O$, $LnCl_3$ and dap under hydrothermal conditions based on the following ideas: (a) The trivacant Keggin-type $[A\text{-}\alpha\text{-}SiW_9O_{34}]^{10-}$ precursor are accessible, which provide us the ample initial material to prepare novel 3d–4f heterometallic STs; (b) the copper ions adopt the flexible coordination geometries such as trigonal bipyramid, square pyramid and octahedron and the obvious Jahn–Teller effect and

* Corresponding authors at: Institute of Molecular and Crystal Engineering, College of Chemistry and Chemical Engineering, Henan University, Kaifeng, Henan 475004, PR China. Tel.: +86 378 3886876; fax: +86 378 3886876.
E-mail addresses: ljchen@henu.edu.cn (L. Chen), zhaojunwei@henu.edu.cn (J. Zhao).

0379-6779/$ – see front matter © 2012 Elsevier B.V. All rights reserved.
http://dx.doi.org/10.1016/j.synthmet.2012.06.020

pseudo-Jahn–Teller effect whereas the Ln cations have the strong oxophilicity and multiple coordination requirements, which favor to combine with the in situ generated ST intermediate phases; (c) because the combination of Ln cations with lacunary STs often leads to precipitation, the hydrothermal method has been untilized to enhance the solubility of all the reactants. Finally, three organic–inorganic hybrid 3d–4f heterometallic ST derivatives, $NaH[Cu(dap)_2(H_2O)][Cu(dap)_2]_{4.5}[Ln(\alpha\text{-}SiW_{11}O_{39})_2]\cdot 7H_2O$ (Ln = Sm^{III} for **1**, Dy^{III} for **2**, Gd^{III} for **3**) have been successfully synthesized. The common features of **1**–**3** are that they are all constructed by 1:2-type $[Ln(\alpha\text{-}SiW_{11}O_{39})_2]^{13-}$ subunits and $[Cu(dap)_2]^{2+}$ bridges. As far as we know, **1**–**3** represent the rare 3D organic–inorganic hybrid ST-based 3d–4f heterometallic derivatives. The luminescence properties of **1** and **2** are mainly derived from the contribution of the Sm^{III} and the Dy^{III} ions. The magnetic properties of **1**–**3** have been measured.

2. Experimental

2.1. Materials and physical measurements

The precursor $Na_{10}[A\text{-}\alpha\text{-}SiW_9O_{34}]\cdot 18H_2O$ was synthesized according to the reference [29] and confirmed by IR spectra. Other chemical reagents were used as purchased without further purification. Elemental analyses (C, H and N) were conducted on a Perkin-Elmer 2400-II CHNS/O elemental analyzer. IR spectra were obtained from a solid sample palletized with KBr on Nicolet FT-IR 360 spectrometer in the range of 4000–400 cm^{-1}. Emission/excitation spectra were recorded on a HITACHI F-7000 fluorescence spectrophotometer. Magnetic susceptibility measurements were carried out with a Quantum Design MPMS-XL-7 magnetometer in the temperature range of 2–300 K. The susceptibility data were corrected from the diamagnetic contributions as deduced by using Pascal's constant tables.

2.2. Synthesis of *1*–*3*

2.2.1. Synthesis of *1*

A mixture of $Na_{10}[A\text{-}\alpha\text{-}SiW_9O_{34}]\cdot 18H_2O$ (0.138 g, 0.049 mmol), $CuCl_2\cdot 2H_2O$ (0.145 g, 0.850 mmol), $SmCl_3$ (0.050 g, 0.195 mmol), dap (0.20 mL, 2.401 mmol), H_2O (5 mL, 278 mmol) and HCl (0.30 mL, 2 mol L^{-1}) (pH_i = 5.3) was stirred for 3 h, sealed in a 25 mL Teflon-lined steel autoclave, kept at 160 °C for 5 days and then slowly cooled to room temperature (pH_f = 4.8). Black prismatic crystals were collected by filtration, washed with distilled water and dried in air at ambient temperature. Yield: ca. 21% (based on $Na_{10}[A\text{-}\alpha\text{-}SiW_9O_{34}]\cdot 18H_2O$). Anal. Calcd. (found %) for $C_{33}H_{127}N_{22}O_{86}NaSmCu_{5.5}Si_2W_{22}$ (**1**): C 5.80 (5.91), H 1.87 (1.99), N 4.51 (4.38).

2.2.2. Synthesis of *2*

A mixture of $Na_{10}[A\text{-}\alpha\text{-}SiW_9O_{34}]\cdot 18H_2O$ (0.130 g, 0.047 mmol), $CuCl_2\cdot 2H_2O$ (0.148 g, 0.868 mmol), $DyCl_3$ (0.053 g, 0.197 mmol), dap (0.15 mL, 1.801 mmol), H_2O (6 mL, 334 mmol) and HCl (0.30 mL, 2 mol L^{-1}) (pH_i = 5.0) was stirred for 3 h, sealed in a 25 mL Teflon-lined steel autoclave, kept at 160 °C for 5 days and then slowly cooled to room temperature (pH_f = 4.6). Purple prismatic crystals were collected by filtration, washed with distilled water and dried in air at ambient temperature. Yield: ca. 25% (based on $Na_{10}[A\text{-}\alpha\text{-}SiW_9O_{34}]\cdot 18H_2O$). Anal. Calcd. (found %) for $C_{33}H_{127}N_{22}O_{86}NaDyCu_{5.5}Si_2W_{22}$ (**2**): C 5.79 (5.95), H 1.87 (2.02), N 4.50 (4.61).

2.2.3. Synthesis of *3*

A mixture of $Na_{10}[A\text{-}\alpha\text{-}SiW_9O_{34}]\cdot 18H_2O$ (0.135 g, 0.048 mmol), $CuCl_2\cdot 2H_2O$ (0.148 g, 0.868 mmol), $GdCl_3$ (0.051 g, 0.193 mmol), dap (0.20 mL, 2.401 mmol), H_2O (4 mL, 222 mmol) and HCl (0.30 mL, 2 mol L^{-1}) (pH_i = 5.3) was stirred for 3 h, sealed in a 25 mL Teflon-lined steel autoclave, kept at 160 °C for 5 days and then slowly cooled to room temperature (pH_f = 4.8). Purple prismatic crystals were collected by filtration, washed with distilled water and dried in air at ambient temperature. Yield: ca. 32% (based on $Na_{10}[A\text{-}\alpha\text{-}SiW_9O_{34}]\cdot 18H_2O$). Anal. Calcd. (found %) for $C_{33}H_{127}N_{22}O_{86}NaGdCu_{5.5}Si_2W_{22}$ (**3**): C 5.80 (5.69), H 1.87 (1.97), N 4.51 (4.39).

2.3. X-ray crystallography

Intensity data for **1**–**3** were collected on a Bruker APEX-II CCD diffractometer using graphite monochromatized Mo Kα radiation (λ = 0.71073 Å) at 296(2) K. Direct methods were used to solve their structures and to locate the heavy atoms using the SHELXTL-97 program package [30,31]. The remaining atoms were found from successive full-matrix least-squares refinements on F^2 and Fourier syntheses. Lorentz polarization and empirical absorption corrections were applied. All non-hydrogen atoms were refined anisotropically. Positions of the hydrogen atoms attached to the carbon and nitrogen atoms were geometrically placed. All

Table 1
Summary of crystallographic data and structure refinements for **1**–**3**.

Data	**1**	**2**	**3**
Empirical formula	$C_{33}H_{127}N_{22}O_{86}NaSmCu_{5.5}Si_2W_{22}$	$C_{33}H_{127}N_{22}O_{86}NaDyCu_{5.5}Si_2W_{22}$	$C_{33}H_{127}N_{22}O_{86}NaGdCu_{5.5}Si_2W_{22}$
Formula weight	6832.26	6844.41	6839.16
Crystal system	Triclinic	Triclinic	Triclinic
Space group	*P*−1	*P*−1	*P*−1
a (Å)	18.297(2)	18.31(3)	18.245(6)
b (Å)	19.911(2)	19.86(3)	19.916(6)
c (Å)	20.270(2)	20.20(4)	20.221(3)
α (°)	87.251(2)	87.28(3)	87.202(7)
β (°)	66.210(2)	66.25(4)	66.248(6)
γ (°)	83.315(2)	83.43(3)	83.332(6)
V (Å^3)	6711.3(13)	6676(20)	6680(3)
Z	2	2	2
D_c (g cm^{-3})	3.381	3.405	3.400
μ (mm^{-1})	20.160	20.385	20.312
Limiting indices	$-21 \le h \le 21$ $-22 \le k \le 23$ $-18 \le l \le 24$	$-11 \le h \le 21$ $-23 \le k \le 23$ $-18 \le l \le 24$	$-21 \le h \le 16$ $-23 \le k \le 23$ $-24 \le l \le 12$
Goodness-of-fit on F^2	1.039	0.980	1.047
R_1, wR_2 [$I > 2\sigma(I)$]	0.0572, 0.1259	0.0700, 0.1540	0.0713, 0.1454
R_1, wR_2 [all data]	0.0866, 0.1345	0.1658, 0.1802	0.1271, 0.1567

hydrogen atoms were refined isotropically as a riding mode using the default SHELXTL parameters. No hydrogen atoms associated with the water molecules were located from the difference Fourier map. Crystal data and structure refinements for **1**–**3** are summarized in Table 1.

3. Results and discussion

3.1. IR spectra

The IR spectra of **1**–**3** have been recorded between 4000 and 400 cm^{-1} with KBr pellets (Fig. 1) and display characteristic vibration patterns derived from the Keggin-type POM framework in the low-wavenumber region. Observably, four groups of the characteristic vibration bands attributable to $\nu(W–O_t)$, $\nu(Si–O_a)$, $\nu(W–O_b)$ and $\nu(W–O_c)$ are observed at 938, 882, 771 and 703 cm^{-1} for **1**, 938, 886, 774 and 702 cm^{-1} for **2**, and 938, 883, 773 and 701 cm^{-1} for **3**, respectively. The similarity of their IR spectra in the low-wavenumber region may result from the presence of the monovacant Keggin-type $[\alpha\text{-}SiW_{11}O_{39}]^{8-}$ fragment in their skeletons. In contrast, their IR spectra are obviously different from that of $Na_{10}[A\text{-}\alpha\text{-}SiW_9O_{34}]\cdot 18H_2O$ (Fig. 1), which further confirms the structural transformation of $[A\text{-}\alpha\text{-}SiW_9O_{34}]^{10-}$ to $[\alpha\text{-}SiW_{11}O_{39}]^{8-}$. Moreover, the characteristic vibration bands of dap ligands are also observed in the IR spectra. The resonance signals at 3286–3125 cm^{-1} and 2963–2873 cm^{-1} are ascribed to the $\nu(NH_2)$ and $\nu(CH_2)$ stretching vibration whereas the bending vibration bands of $\nu(NH_2)$ and $\nu(CH_2)$ appear at 1635–1582 cm^{-1} and 1457–1396 cm^{-1}. Additionally, the vibration band at 3437–3450 cm^{-1} is indicative of the presence of water molecules. In conclusion, the results of the IR spectra are good agreement with the X-ray single-crystal structural analyses.

3.2. Structural description

X-ray diffraction structural analyses reveal that **1**–**3** are isomorphous and crystallize in the triclinic space group $P\bar{1}$. Furthermore, they all exhibit the scarce 3D frameworks built up from $[Ln(\alpha\text{-}SiW_{11}O_{39})_2]^{13-}$ (Ln = Sm^{III} for **1**, Dy^{III} for **2**, Gd^{III} for **3**) subunits and $[Cu(dap)_2]^{2+}$ cations. Therefore, only the structure of **1** is discussed in detail here. The molecular structural unit of **1** consists

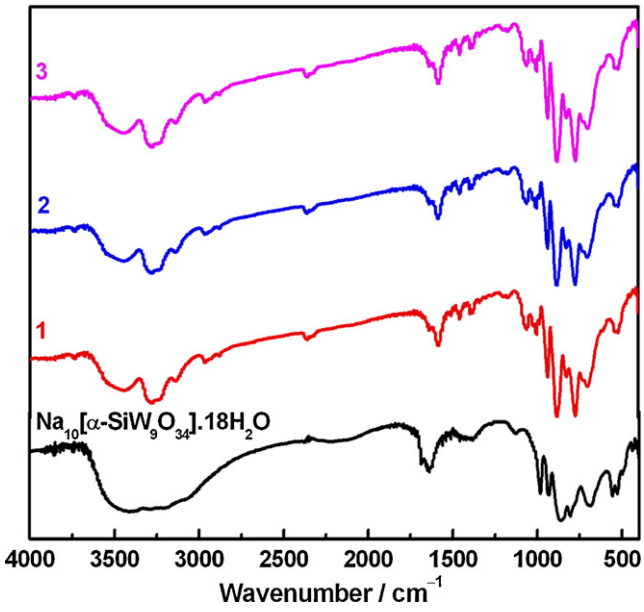

Fig. 1. Comparison of the IR spectra of **1**–**3** and $Na_{10}[A\text{-}\alpha\text{-}SiW_9O_{34}]\cdot 18H_2O$.

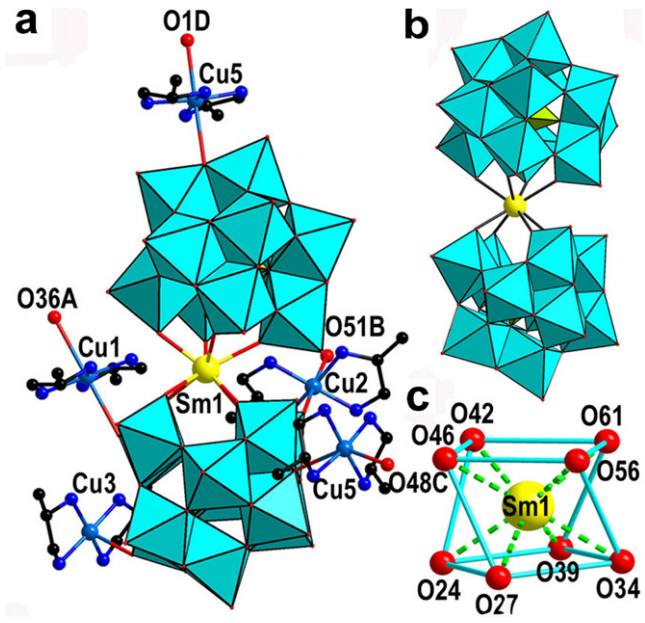

Fig. 2. (a) Combined polyhedral/ball-and-stick representation of **1** with selected numbering scheme. The atoms with "A, B, C, D" in their labels are symmetrically generated (A: $-x, -y, 1-z$; B: $-x, 1-y, 1-z$; C: $-1-x, 1-y, 1-z$; D: $1+x, y, -1+z$). (b) The polyhedral view of the 1:2-type $[Sm(\alpha\text{-}SiW_{11}O_{39})_2]^{13-}$ unit. (c) The distorted square antiprismatic configuration of the Sm^{III} in **1** constituted by eight O atoms from the vacant sites of two adjacent $[\alpha\text{-}SiW_{11}O_{39}]^{8-}$ moieties.

of 1 1:2-type $[Sm(\alpha\text{-}SiW_{11}O_{39})_2]^{13-}$ fragment, 4.5 $[Cu(dap)_2]^{2+}$ cations, 1 free $[Cu(dap)_2(H_2O)]^{2+}$ cation, 1e Na^+ cation, 1 H^+ proton and 7 lattice water molecules (Fig. 2a). In **1**, there are six crystallographically independent Cu^{II} cations (Cu1, Cu2, Cu3, Cu4, Cu5 and Cu6), in which the Cu1 cation is situated on the special position with the site occupancy factor of 0.5 while the remaining copper cations occupy the usual sites with the site occupancy factor of 1 for each. The bridging $[Cu1(dap)_2]^{2+}$, $[Cu2(dap)_2]^{2+}$, $[Cu5(dap)_2]^{2+}$ and $[Cu6(dap)_2]^{2+}$ cations all exhibit the six-coordinate octahedral geometry, in which four N atoms from two dap ligands build the basal plane [Cu—N: 1.965(14)–2.05(2) Å], two O atoms from two adjacent $[Sm(\alpha\text{-}SiW_{11}O_{39})_2]^{13-}$ fragments [Cu—O: 2.387(14)–2.855(13) Å] occupy two axial positions. To be more specific, two axial O atoms on the $[Cu1(dap)_2]^{2+}$ and $[Cu2(dap)_2]^{2+}$ cations come from the terminal O atoms of the adjacent different $[Sm(\alpha\text{-}SiW_{11}O_{39})_2]^{13-}$ fragments, two axial O atoms on the $[Cu5(dap)_2]^{2+}$ cation are from two bridging O atoms of the adjacent different $[Sm(\alpha\text{-}SiW_{11}O_{39})_2]^{13-}$ fragments and two axial O atoms on the $[Cu6(dap)_2]^{2+}$ cation are derived from one terminal O atom and one bridging O atom. The pendent $[Cu3(dap)_2]^{2+}$ and free $[Cu4(dap)_2(H_2O)]^{2+}$ cations exhibit the square pyramid geometry established by four N atoms from dap ligands with Cu—N bond lengths ranging from 1.966(16) to 2.054(17) Å and one terminal/water O atom with Cu—O bond lengths of 2.359(13)–2.465(19) Å. The 1:2-type $[Sm(\alpha\text{-}SiW_{11}O_{39})_2]^{13-}$ subunit is constituted by an eight-coordinate Sm^{III} cation sandwiched by two monolacunary $[\alpha\text{-}SiW_{11}O_{39}]^{8-}$ moieties resulting in a well-known sandwich-type bis(undecatungstosilicate)lanthanate structure (Fig. 2b). Such 1:2-type structural type was firstly discovered by Peacock and Weakly in 1971 [10] and this 1:2 structural series made up of one Ln cation and two monovacant Keggin-type POM units have been widely investigated [32,33]. In the $[Sm(\alpha\text{-}SiW_{11}O_{39})_2]^{13-}$ subunit, the Sm^{III} cation adopts a distorted square antiprismatic configuration defined by eight O atoms (O42, O46, O56, O61, O24, O27, O34, O39) from the vacant sites of two adjacent $[\alpha\text{-}SiW_{11}O_{39}]^{8-}$ moieties with Sm—O distances of 2.397(10)–2.433(11) Å and their average of 2.417 Å (Fig. 2c). In the

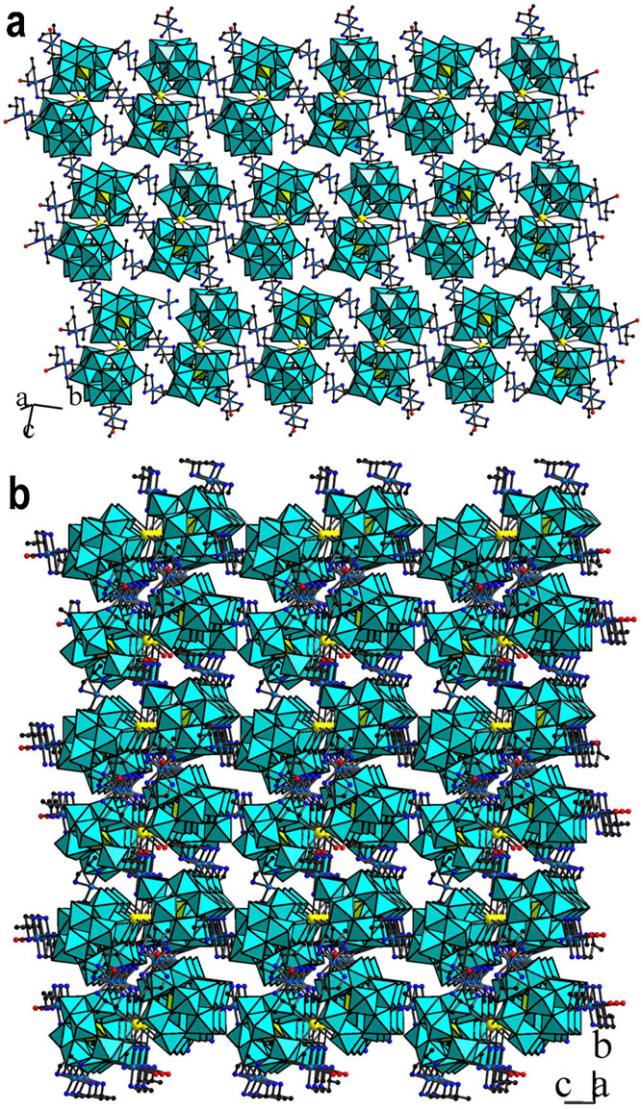

Fig. 3. (a) The 2-D sheet constructed from $[Sm(\alpha\text{-}SiW_{11}O_{39})_2]^{13-}$ units linked by $[Cu1(dap)_2]^{2+}$, $[Cu3(dap)_2]^{2+}$, $[Cu5(dap)_2]^{2+}$ and $[Cu6(dap)_2]^{2+}$ bridges. (b) The resulting 3D 3d–4f heterometallic POM framework.

coordination polyhedron around the Sm^{III} cation, O42, O46, O56, O61 group and O24, O27, O34, O39 group constitute two bottom planes of the square antiprism and their standard deviations from their least-squares planes are 0.0022 and 0.0091 Å, respectively. The dihedral angle for the two bottom surfaces is 1.8°. The distances of the Sm^{III} cation and two bottom surfaces are 1.2776 and 1.3045 Å, respectively. The above-mentioned data indicate that the square antiprism is severely distorted. In the $[Sm(\alpha\text{-}SiW_{11}O_{39})_2]^{13-}$ subunit, the Si atoms reside in the center of SiO_4 tetrahedra, which have been somewhat distorted resulting from the removal of one $[W=O_t]^{4+}$ unit and the incorporation of the Sm^{III} cation into the monovacant POM subunit as compared to the saturated Keggin-type structure. The Si—O bond lengths vary from 1.587(12) to 1.636(11) Å, and the O—Si—O bond lengths are in the range of 107.6(6)–112.7(6) Å. Similarly, all the WO_6 octahedra are distorted to some degree.

It is worth noting that adjacent $[Sm(\alpha\text{-}SiW_{11}O_{39})_2]^{13-}$ units are linked together by $[Cu1(dap)_2]^{2+}$, $[Cu3(dap)_2]^{2+}$, $[Cu5(dap)_2]^{2+}$, $[Cu6(dap)_2]^{2+}$ bridging cations giving rise to the 2D sheet structure (Fig. 3a). More intriguingly, adjacent 2D sheets are interconnected through the $[Cu2(dap)_2]^{2+}$ cations constructing a fascinating 3D framework (Fig. 3b). As far as we know, such organic–inorganic hybrid 3D 3d–4f heterometallic STs are very scarce up to now except that two examples of $(enH_2)_2\{[Cu(en)_2(H_2O)][Cu(en)_2]_2Pr[(\alpha\text{-}H_{1.5}SiW_{11}O_{39})_2]\}\cdot 6H_2O$ and $(enH_2)\{[Cu(en)_2(H_2O)][Cu(Hen)_2][Cu(en)_2]_2Sm[(\alpha\text{-}H_{0.5}SiW_{11}O_{39})_2]\}\cdot 6H_2O$ have been recently reported by Niu and coworkers [27]. From the topological point of view, the circuit symbols Schläfli (vertex) notations can be used to describe topologies and facilitate comparison of networks of different composition and metrics [34]. If each $[Cu(dap)_2(H_2O)][Cu(dap)_2]_{4.5}[Sm(\alpha\text{-}SiW_{11}O_{39})_2]^{2-}$ unit is considered as a 5-connected node (Fig. 4a), the 3D framework of **1** can be described as a 5-connected 3D network with the short vertex (Schläfli) symbol of $(4^6\cdot 6^4)$ (Fig. 4b) and the long topological (O'Keeffe) vertex symbol of $(6\cdot 6\cdot 4\cdot 4\cdot 6\cdot 4\cdot 4\cdot 4\cdot 4\cdot 6_3)$.

3.3. Photoluminescence properties

Trivalent Ln cations display unique photophysical properties including sharp and characteristic transitions in the visible or near-infrared regions. Generally, the Ln cations, when directly excited, can exhibit weak emission because of the low molar absorption coefficient resulting from the Laporte forbidden *f–f* transitions [35]. The Ln cations with energy levels suitable for emitting visible light are Sm^{III}, Eu^{III}, Tb^{III}, Dy^{III} and Tm^{III}, with Eu^{III} (red emission) and Tb^{III} (green emission) the most extensively studied because of their longer emission lifetimes [35]. As they can exhibit extremely sharp emission bands attributed to their 4*f* electrons, Ln elements have always played a prominent role in lighting and light conversion technologies such as lasers, light-emitting diodes and cathode ray tubes [36]. It was realized that the peculiar luminescent properties of Ln complexes can be exploited in extensive applications, such as biomedical, sensing areas and luminescence imaging for their high color purity and potentially high internal quantum efficiency in coordination chemistry [37]. Therefore, the solid-state photoluminescence properties of **1**–**3** are measured at room temperature upon photoexcitation and only **1**–**2** display the weak photoluminescence. Low emission intensities at room temperature for some Ln-POMs are mainly attributed to radiationless deactivation via Ln^{IV}–W^{V} charge-transfer states [35]. Excited at 302 nm at room temperature, **1** reveals three characteristic emission bands of the Sm^{III} cation at 576, 605 and 635 nm, which originate from the $^4G_{5/2} \rightarrow {}^6H_{5/2}$, $^4G_{5/2} \rightarrow {}^6H_{7/2}$ and $^4G_{5/2} \rightarrow {}^6H_{9/2}$ transitions, respectively (Fig. 5a), being in good accordance to the previous results [38]. Excitation of the as-synthesized solid of **2** at 285 nm yields the characteristic emission bands of the Dy^{III} ion (Fig. 5b). Two characteristic bands can be seen at 493 and 572 nm in the emission spectrum of **2**, which are respectively attributed to the $^4F_{9/2} \rightarrow {}^6H_{15/2}$ and $^4F_{9/2} \rightarrow {}^6H_{13/2}$ transitions of the Dy^{III} cation. The $^4F_{9/2} \rightarrow {}^6H_{15/2}$ transition clearly split into double peaks, which may be the result of the Stark sublevel splitting from the $^6H_{15/2}$ energy level by the ligand field [38]. The mechanism of energy transfer from the ligand to the metal has been widely discussed to interpret the luminescence of Ln-complexes [39–41]. When the triplet-state energy of the ligand is greater than or equal to the energy gap (ΔE) between the excited state and ground state of the metal ion, efficient luminescence could be obtained [42,43]. From the results discussed above, we could presume that the energy gap (ΔE) of the Sm^{III} cation may be smaller than that of the Dy^{III} cation. It means that the ligand-to-metal charge transfer of the Sm^{III} cation is more effective than that of the Dy^{III} cation.

3.4. Magnetic properties

In recent years, 3d–4f heterometallic complexes have attracted a growing interest due to the presence of exchange interactions

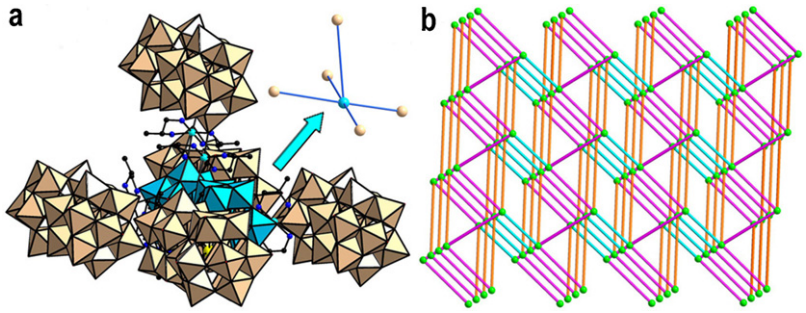

Fig. 4. (a) The combination of each $[Cu(dap)_2(H_2O)][Cu(dap)_2]_{4.5}[Sm(\alpha\text{-}SiW_{11}O_{39})_2]^{2-}$ unit with adjacent five same ones. (b) The topology structure of **1**.

between spin carriers in the solid-state chemistry and material science [44,45]. As a result, the magnetic susceptibilities of **1**–**3** have been measured for polycrystalline sample in the temperature range of 2–300 K at an applied field of 2000 Oe and the plots of χ_M, $\chi_M T$ and $\chi_M{}^{-1}$ versus T are shown in Figs. 6–8. Since the orbital contribution occurs for the most Ln cations and the ligand field effect on the magnetic characteristics of the cations displays the spin–orbit coupling, not much is known about the nature and magnitude of the coupling in the Ln-complexes and the evolution of the magnetic properties along the Ln series [46]. In general, the ^{2S+1}L group term of the $4f^n$ configuration for a Ln cation is often split into $^{2S+1}L_J$ spectroscopic levels by interelectronic repulsion and spin–orbit coupling. Each of these states is further split into Stark sublevels by the crystal field perturbation [46,47]. Therefore, the major difficulty in analyzing the magnetic properties of the 3d–4f hetrometallic complexes lies in the case that the ground state of the Ln cations (Ln ≠ La^{III}, Gd^{III}, Lu^{III}) has a first-order angular momentum, preventing the use of the spin-only isotropic Hamiltonian [48–50]. At room temperature, all Stark sublevels of the $^{2S+1}L_J$ ground state or those of the low-lying first excited states for Sm^{III} and Eu^{III} cations are thermally populated.

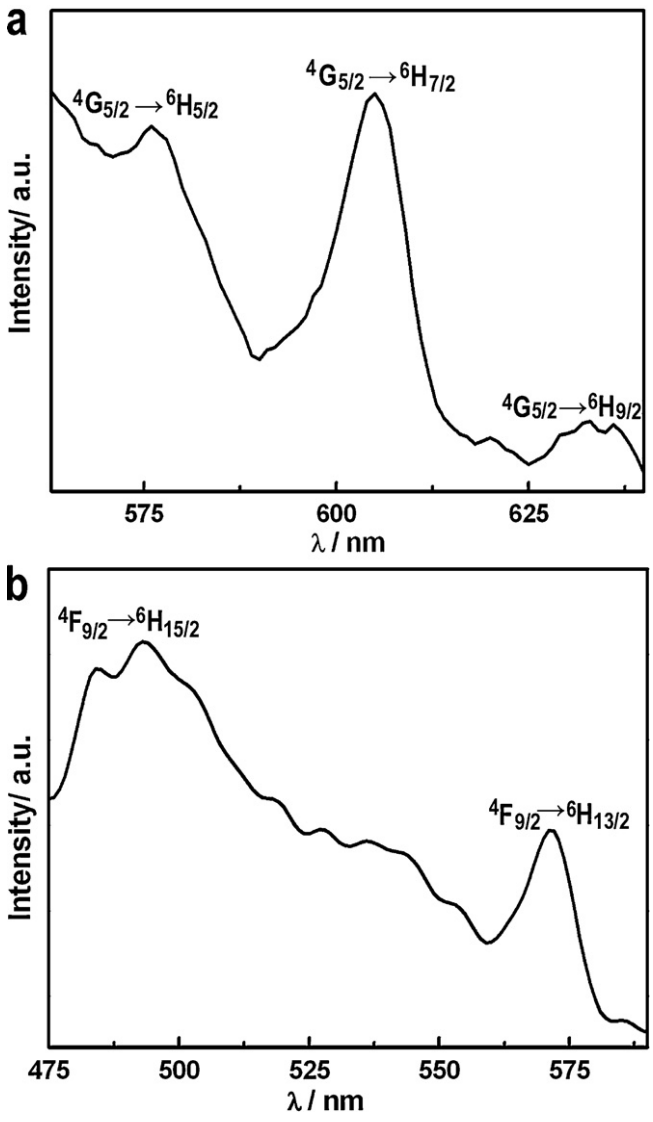

Fig. 5. (a) The solid-state emission spectrum of **1** at room temperature (λ_{ex} = 302 nm). (b) The solid-state emission spectrum of **2** at room temperature (λ_{ex} = 285 nm).

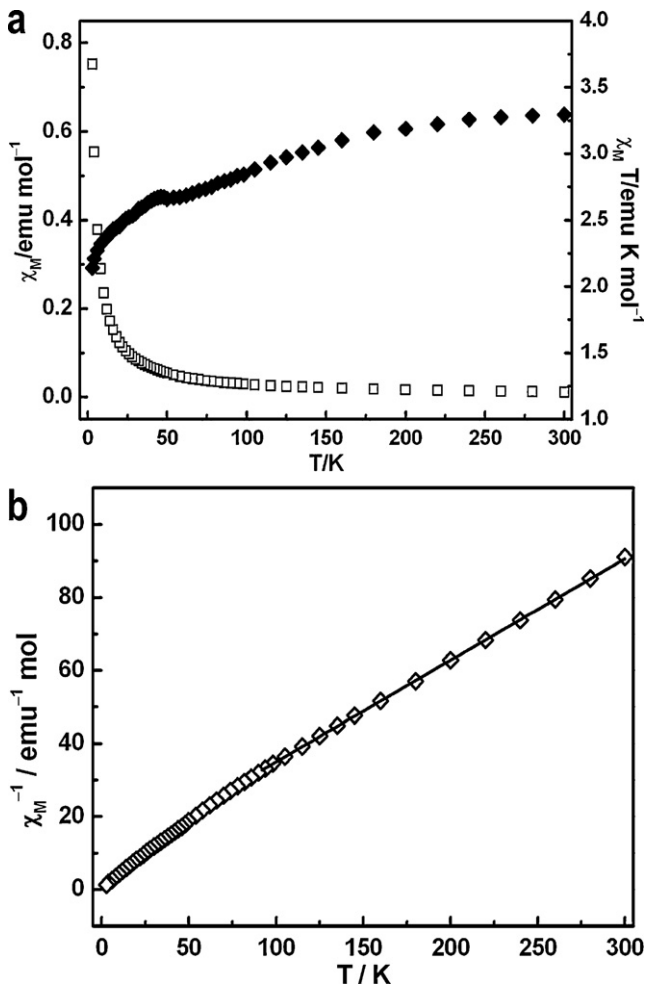

Fig. 6. (a) and (b) Plots of the temperature dependence of χ_M, $\chi_M T$ and $\chi_M{}^{-1}$ for **1**. The solid line in b is generated from the best fit by the Curie–Weiss expression.

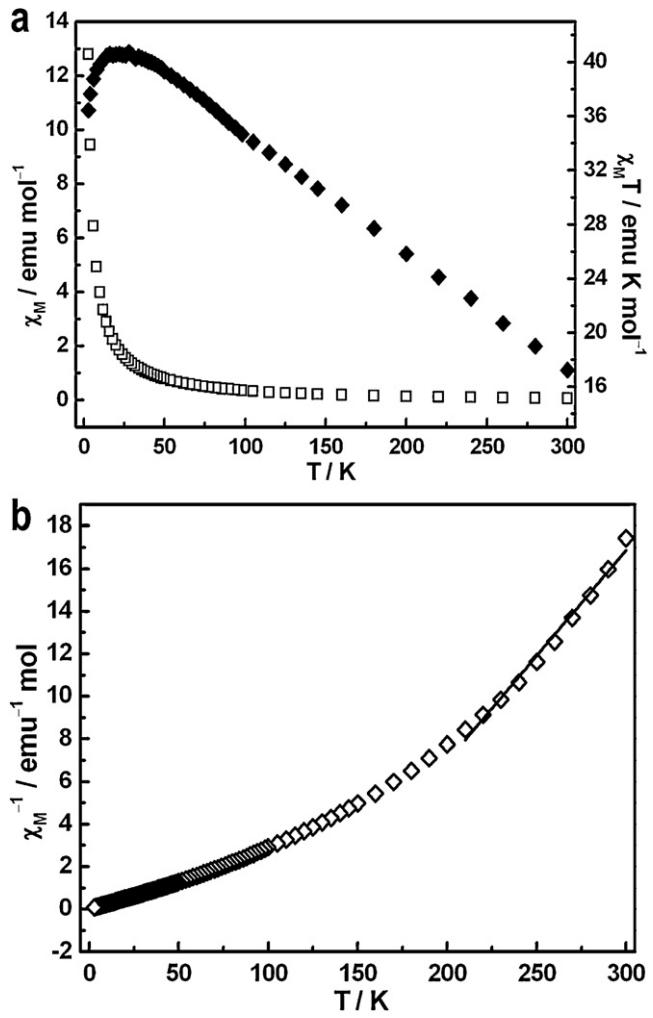

Fig. 7. (a) and (b) Plots of the temperature dependence of χ_M, $\chi_M T$ and $\chi_M{}^{-1}$ for **2**. The solid line in d is generated from the best fit by the Curie–Weiss expression.

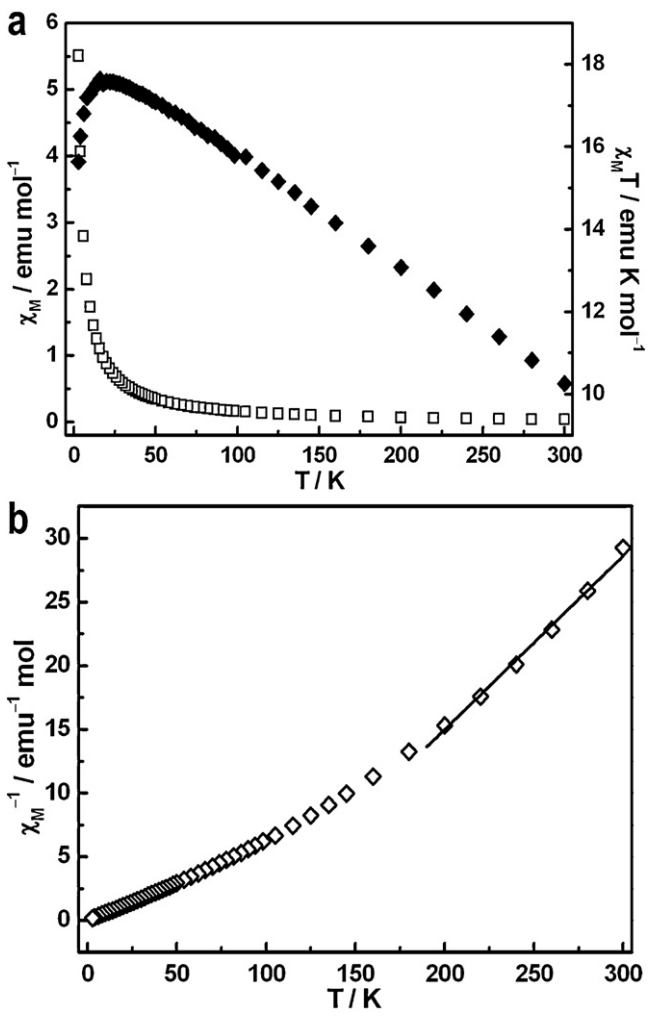

Fig. 8. (a) and (b) Plots of the temperature dependence of χ_M, $\chi_M T$ and $\chi_M{}^{-1}$ for **3**. The solid line in f is generated from the best fit by the Curie–Weiss expression.

As the temperature drops, a depopulation of these sublevels occurs and consequently the $\chi_M T$ decreases. The temperature dependence of the χ_M deviates with respect to the Curie–Weiss law [46,48]. Thus, the magnetic properties of **1**–**3** are preliminarily investigated. For **1**, the temperature dependence of the χ_M shows a slight increase from 0.01 emu mol^{-1} to 0.09 emu mol^{-1} from 300 to 27 K. This tendency becomes more pronounced below 27 K, leading to an exponential increase between 27 and 2 K. Finally, a sharp increase reaches 0.75 emu mol^{-1} (Fig. 6a). The $\chi_M T$ value decreases from 3.29 emu K mol^{-1} at 300 K to 2.14 emu K mol^{-1} at 2 K when the temperature is lowered. The $\chi_M T$ value at 300 K is evidently higher than the contribution (2.15 emu K mol^{-1}) corresponding to 5.5 uncoupling Cu^{II} cations ($S = 1/2$) with $g = 2.00$ and 1 free Sm^{III} cation in the $^6H_{5/2}$ group state ($J = 5/2$, $g = 2/7$) [51], which reveals the occurrence of the spin–orbital coupling and the crystal field effect. The $^6H_{5/2}$ ground state for the free Sm^{III} cation in the crystal field is split into six states by spin–orbit coupling, and the spin–orbit coupling parameter is 1200 cm^{-1}, so the crystal field effect and the possible thermal population of the high energy states should be considered for **1** [52]. The curve of $\chi_M{}^{-1}$ versus T in 300–93 K can be described using the Curie–Weiss law [$\chi = C/(T-\theta)$, C is the Curie constant, and θ is the Curie–Weiss temperature] affording the Curie constant $C = 3.60$ emu K mol^{-1} (Fig. 6b) and the Weiss constant $\theta = -25.79$ K, but the relation of $\chi_M{}^{-1}$ versus T between 93 and 2 K somewhat deviates from the Curie–Weiss law that is caused by first- and second-order Zeeman effect contributions of the ground ($^6H_{5/2}$) and first excited ($^6H_{7/2}$) states of the Sm^{III} cation, which are close in energy and thermally populated at room temperature because of the relatively low spin–orbit coupling effect [53]. For **2**, the value of χ_M gradually increases from 0.06 emu mol^{-1} at 300 K to 1.69 emu mol^{-1} at 24 K, and then sharply reaches to the maximum value of 12.80 emu mol^{-1} at 2 K (Fig. 7a). The value of $\chi_M T$ at 300 K is 17.22 emu mol^{-1} K, being slightly higher than the sum (16.23 emu K mol^{-1}) of the contribution attributable to 5.5 non-interacting Cu^{II} cations ($S = 1/2$) with $g = 2.00$ and 1 free Dy^{III} cation in the $^6H_{15/2}$ group state ($J = 15/2$, $g = 4/3$) [41,54,55]. The $\chi_M T$ increases to a maximum of 40.72 emu mol^{-1} K at 28 K upon cooling. This behavior of the $\chi_M T$ versus T plot illustrates the ferromagnetic coupling interactions. Fitting the high-temperature susceptibility ($205 < T < 300$) to the Curie–Weiss law results in values of $C = 10.09$ emu K mol^{-1} and $\theta = 129.87$ K (Fig. 7b), which is consistent with the ferromagnetic coupling interactions. The decrease in $\chi_M T$ on decreasing the temperature from 28 to 2 K can be ascribed to the intermolecular antiferromagnetic interactions and the thermal depopulation of Stark sublevels of the Dy^{III} cations [56,57]. Generally, the Dy^{III} cation with a first-order orbital momentum has the $^6H_{15/2}$ ground state, which is split into eight Stark components in the low symmetrical crystal field, each of them being a Kramers doublet. The energy gap between highest and lowest Kramers doublets is on the order of a few hundreds of wavenumbers [58]. Upon cooling, the highest Kramers doublets are progressively depopulated, and at 2 K only the ground Kramers doublet is populated.

This situation often results in the pronounced deviation of the magnetic behavior from the Curie law (Fig. 7b). For **3**, the χ_M gradually rises from 0.03 emu mol^{-1} at 300 K to 0.56 emu mol^{-1} at 31 K, then exponentially to the maximum of 5.52 emu mol^{-1} at 2 K (Fig. 8a). At 300 K, the $\chi_M T$ is equal to 10.25 emu mol^{-1} K, which is good agreement with that expected value (9.93 emu mol^{-1} K) for 5.5 magnetically uncoupled Cu^{II} cations assuming $g = 2$ and 1 free Gd^{III} cation in the $^8S_{7/2}$ group state ($J = 7/2$, $g = 1.993$) [55]. It should be noted that the reduced g value of 1.993 is a result of the large spin–orbit interaction that mixes significant amounts of other terms into the $J = 7/2$ ground state. The major Russell–Saunders components of the ground state are ^8S (97%) and ^6P (2.7%), affording a g factor of 1.993 [55,59,60]. When the sample is cooled from 300 K to 20 K, the $\chi_M T$ gradually increases to reach a maximum of 17.59 emu mol^{-1} K at 20 K before dropping to 15.63 emu mol^{-1} K at 2 K. This behavior is indicative of the presence of the ferromagnetic exchange interactions. The inverse magnetic susceptibility data in the temperature range of 188–300 K are fitted to the Curie–Weiss equation with $C = 7.33$ emu mol^{-1} K and $\theta = 90.04$ K (Fig. 8b). The positive Weiss constant also suggests the occurrence of the ferromagnetic interactions. The decrease of $\chi_M T$ observed below 20 K is most likely attributable to the saturation effects [55,61]. Actually, Costes et al. have already investigated the nature of the overall Cu–Ln magnetic interactions and concluded that the Cu–Ln interactions are antiferromagnetic when Ln = Ce^{III}, Nd^{III}, Sm^{III}, Tm^{III}, Yb^{III}, while the Cu–Ln interactions are ferromagnetic when Ln = Gd^{III}, Tb^{III}, Dy^{III}, Ho^{III}, Er^{III}, and as for Cu^{II}–Pr^{III} and Cu^{II}–Eu^{III} complexes, the Pr^{III} and Eu^{III} cations are nonmagnetic at the low temperature [62]. As discussed above, the Cu–Ln interactions in **1**–**3** agree with the conclusions made by Costes [62].

4. Conclusion

Three organic–inorganic hybrid 3d–4f heterometallic STs **1**–**3** have been successfully prepared under hydrothermal conditions and exhibit unique 3D 5-connected ($4^6.6^4$) framework topology based on 1:2-type $[Ln(\alpha\text{-}SiW_{11}O_{39})_2]^{13-}$ subunits and $[Cu(dap)_2]^{2+}$ cation bridges. As far as we know, they represent the rare 3D organic–inorganic hybrid Keggin ST-based 3d–4f heterometallic derivatives. The successful isolations of **1**–**3** suggest that one-pot reaction self-assembly of lacunary POM precursors, Ln salts, TM salts and organic ligands is an effective strategy in constructing 3d–4f heterometallic POM hybrids. The luminescence properties of **1**–**2** have been investigated and are mainly derived from the contribution of the Sm^{III} and the Dy^{III} ions. Furthermore, the magnetic susceptibilities of **1**–**3** have been measured and preliminarily analyzed. Further work in this area will be focused on making other novel 3d–4f heterometallic POMs with unexpected structures and properties by introducing organic polycarboxylic ligands or the chiral organic ligands to the reaction system.

Supplementary data

Electronic Supplementary Information (ESI) available: Crystallographic data have been deposited with the Cambridge Crystallographic Data Center as supplementary publication CCDC 873583, 873584 and 873585. Copies of the data can be obtained free of charge on application to CCDC, 12 Union Road, Cambridge CB2 1EZ, UK (fax: +44 1223 336 033, deposit@ccdc.cam.ac.uk).

Acknowledgements

We are thankful for financial support from the Natural Science Foundation of China (Nos. 21101055, 21071042 and 21071043), China Postdoctoral Science Foundation funded project (Nos. 201104392 and 20100470996), the Natural Science Foundation of Henan Province (No. 122300410106), the Science Foundation of the State Key Laboratory of Structural Chemistry (No. 20120013), the Postdoctoral Science Foundation of Henan University (No. BH2010003) and the Foundation of Education Department of Henan Province (Nos. 2009A150003 and 2010B150006).

References

[1] P. Mialane, A. Dolbecq, L. Lisnard, A. Mallard, J. Marrot, F. Sécheresse, Angewandte Chemie International Edition 41 (2002) 2398.
[2] U. Kortz, N.K. Al-Kassem, M.G. Savelieff, N.A. Al Kadi, M. Sadakane, Inorganic Chemistry 40 (2001) 4742.
[3] J.J. Borrás-Almenar, E. Coronado, A. Müller, M.T. Pope, Polyoxometalate Molecular Science, Kluwer, Dordrecht, The Netherlands, 2003.
[4] B.S. Bassil, M.H. Dickman, I. Römer, B. von der Kammer, U. Kortz, Angewandte Chemie International Edition 46 (2007) 6192.
[5] S.Z. Li, J.W. Zhao, P.T. Ma, J. Du, J.Y. Niu, J.P. Wang, Inorganic Chemistry 48 (2009) 9819.
[6] L.S. Felices, P. Vitoria, J.M. Gutiérrez-Zorrilla, L. Lezama, S. Reinoso, Inorganic Chemistry 45 (2006) 7748.
[7] D.E. Katsoulis, M.T. Pope, Journal of the American Chemical Society 106 (1984) 2737.
[8] F. Hussain, B.S. Bassil, L.H. Bi, M. Reicke, U. Kortz, Angewandte Chemie International Edition 43 (2004) 3485.
[9] S.T. Zheng, D.Q. Yuan, H.P. Jia, J. Zhang, G.Y. Yang, Chemical Communications (2007) 1858.
[10] R.D. Peacock, T.J.R. Weakley, Journal of the Chemical Society A (1971) 1836.
[11] M. Sadakane, M.H. Dickman, M.T. Pope, Angewandte Chemie International Edition in English 39 (2000) 2914.
[12] J.F. Cao, S.X. Liu, R.G. Cao, L.H. Xie, Y.H. Ren, C.Y. Gao, L. Xu, Dalton Transactions (2008) 115.
[13] W.L. Chen, Y.G. Li, Y.H. Wang, E.B. Wang, Z.M. Zhang, Dalton Transactions (2008) 865.
[14] B. Li, J.W. Zhao, S.T. Zheng, G.Y. Yang, Journal of Cluster Science 20 (2009) 503.
[15] J.P. Wang, Q.X. Yan, X.D. Du, J.Y. Niu, Journal of Cluster Science 19 (2008) 491.
[16] D.Y. Shi, L.J. Chen, J.W. Zhao, Y. Wang, P.T. Ma, J.Y. Niu, Inorganic Chemistry Communications 14 (2011) 324.
[17] J.Y. Niu, S.W. Zhang, H.N. Chen, J.W. Zhao, P.T. Ma, J.P. Wang, Crystal Growth Design 11 (2011) 3769.
[18] S. Reinoso, Dalton Transactions 40 (2011) 6610.
[19] S. Yao, Z.M. Zhang, Y.G. Li, Y. Lu, E.B. Wang, Z.M. Su, Crystal Growth Design 10 (2010) 135.
[20] Y.W. Li, Y.G. Li, Y.H. Wang, X.J. Feng, Y. Lu, E.B. Wang, Inorganic Chemistry 48 (2009) 6452.
[21] A. Merca, A. Müller, J.V. Slageren, M. Läge, B. Krebs, Journal of Cluster Science 18 (2007) 711.
[22] W.L. Chen, Y.G. Li, Y.H. Wang, E.B. Wang, European Journal of Inorganic Chemistry (2007) 2216.
[23] Z.M. Zhang, Y.G. Li, W.L. Chen, E.B. Wang, X.L. Wang, Inorganic Chemistry Communications 11 (2008) 879.
[24] Z.M. Zhang, Y.G. Li, S. Yao, E.B. Wang, Dalton Transactions (2011) 6475.
[25] B. Nohra, P. Mialane, A. Dolbecq, E. Rivière, J. Marrot, F. Sécheresse, Chemical Communications (2009) 2703.
[26] J.D. Compain, P. Mialane, A. Dolbecq, I.M. Mbomekallé, J. Marrot, F. Sécheresse, C. Duboc, E. Rivière, Inorganic Chemistry 49 (2010) 2851.
[27] S.W. Zhang, J.W. Zhao, P.T. Ma, H.N. Chen, J.Y. Niu, J.P. Wang, Crystal Growth Design 12 (2012) 1263.
[28] S.W. Zhang, J.W. Zhao, P.T. Ma, J.Y. Niu, J.P. Wang, Chemistry, An Asian Journal 7 (2012) 966.
[29] G. Hervé, A. Tézé, Inorganic Chemistry 16 (1977) 2115.
[30] G.M. Sheldrick, SHELXS-97, Program for Crystal Structure Solution, University of Göttingen, Göttingen, Germany, 1997.
[31] G.M. Sheldrick, SHELXL-97, Program for Crystal Structure Refinement, University of Göttingen, Göttingen, Germany, 1997.
[32] P. Mialane, L. Lisnard, A. Mallard, J. Marrot, E. Antic-Fidancev, P. Aschehoug, D. Vivien, F. Seïcheresse, Inorganic Chemistry 42 (2003) 2102.
[33] B.S. Bassil, M.H. Dickman, B. von der Kammer, U. Kortz, Inorganic Chemistry 46 (2007) 2452.
[34] B. Moulton, H. Abourahma, M.W. Bradner, J.J. Lu, G.J. McManus, M.J. Zaworotko, Chemical Communications (2003) 1342.
[35] C. Ritchie, V. Baslon, E.G. Moore, C. Reber, C. Boskovic, Inorganic Chemistry 51 (2012) 1142.
[36] L. Armelao, S. Quici, F. Barigelletti, G. Accorsi, G. Bottaro, M. Cavazzini, E. Tondello, Coordination Chemistry Reviews (2010) 254.
[37] Y. Li, F.K. Zheng, X. Liu, W.Q. Zou, G.C. Gou, C.Z. Lu, J.S. Huang, Inorganic Chemistry 45 (2006) 6308.
[38] J. Xia, B. Zhao, H.S. Wang, W. Shi, Y. Ma, H.B. Song, P. Cheng, D.Z. Liao, S.P. Yan, Inorganic Chemistry 46 (2007) 3450.
[39] R.M. Supkowski, J.P. Bolender, W.D. Smith, L.E.L. Reynolds, W.D. Horrocks, Coordination Chemistry Reviews 185–186 (1999) 307.
[40] A. Beeby, S. Faulkner, D. Parker, J.A.G. Williams, Journal of the Chemical Society – Perkin Transactions 2 (2001) 1268.

[41] Z.H. Zhang, Y. Song, T. Okamura, Y. Hasegawa, W.Y. Sun, N. Ueyama, Inorganic Chemistry 45 (2006) 2896.
[42] C. Benelli, D. Gatteschi, Chemical Reviews 102 (2002) 2369.
[43] B. Liu, B.L. Li, Y.Z. Li, Y. Chen, S.S. Bao, L.M. Zheng, Inorganic Chemistry 46 (2007) 8524.
[44] S. Wang, Z. Pang, K.D.L. Smith, M.J. Wagner, Journal of the Chemical Society – Dalton Transactions (1994) 955.
[45] A.C. Rizzi, R. Calvo, R. Baggio, M.T. Garland, O. Peña, M. Perec, Inorganic Chemistry 41 (2002) 5609.
[46] M.L. Kahn, J. Sutter, S. Golhen, P. Guionneau, L. Ouahab, O. Kahn, D. Chasseau, Journal of the American Chemical Society 122 (2000) 3413.
[47] Y. Li, F.K. Zheng, X. Liu, W.Q. Zou, G.C. Guo, C.Z. Lu, J.S. Huang, Inorganic Chemistry 45 (2006) 6308.
[48] J.P. Costes, F. Dahan, A. Dupuis, J.P. Laurent, Chemistry A European Journal 4 (1998) 1616.
[49] Z.H. Zhang, T. Okamura, Y. Hasegawa, H. Kawaguchi, L.Y. Kong, W.Y. Sun, N. Ueyama, Inorganic Chemistry 44 (2005) 6219.
[50] X.J. Zheng, C.Y. Sun, S.Z. Lu, F.H. Liao, S. Gao, L.P. Jin, European Journal of Inorganic Chemistry (2004) 3262.
[51] N. Xu, C. Wang, W. Shi, S.P. Yan, P. Cheng, D.Z. Liao, European Journal of Inorganic Chemistry (2011) 2387.
[52] M. Andruh, E. Bakalbassis, O. Kahn, J.C. Trombe, P. Porcher, Inorganic Chemistry 32 (1993) 1616.
[53] H.Z. Kou, S. Gao, X.L. Jin, Inorganic Chemistry 40 (2001) 6295.
[54] N. Ishikawa, M. Sugita, T. Okubo, N. Tanaka, T. Lino, Y. Kaizu, Inorganic Chemistry 42 (2003) 2440.
[55] C. Ritchie, M. Speldrich, R.W. Gable, L. Sorace, P. Kögerler, C. Boskovic, Inorganic Chemistry 50 (2011) 7004.
[56] K.C. Mondal, G.E. Kostakis, Y. Lan, W. Wernsdorfer, C.E. Anson, A.K. Powell, Inorganic Chemistry 50 (2011) 11604.
[57] J. Rinck, G. Novitchi, W.V.d. Heuvel, L. Ungur, Y. Lan, W. Wernsdorfer, C.E. Anson, L.F. Chibotaru, A.K. Powell, Angewandte Chemie International Edition 49 (2010) 7583.
[58] M.L. Kahn, C. Mathonière, O. Kahn, Inorganic Chemistry 38 (1999) 3692.
[59] J. Sytsma, K.M. Murdoch, N.M. Edelstein, L.A. Boatner, M.M. Abraham, Physical Review B 52 (1995) 12668.
[60] A.J. Shuskus, Physical Review 127 (1962) 2022.
[61] J.P. Costes, F. Dahan, A. Dupuis, J.P. Laurent, Inorganic Chemistry 35 (1996) 2400.
[62] J.P. Costes, F. Dahan, A. Dupuis, J.P. Laurent, Chemistry An Asian Journal 4 (1998) 1616.